Numerical Simulation of Focused Wave Interaction with WEC Models using qaleFOAM

Author 1

- Junxian Wang, Msc
- School of Mathematics, Computer Science and Engineering, City, University of London,UK

Author 2

- Shiqiang Yan, Ph.D
- School of Mathematics, Computer Science and Engineering, City, University of London, UK
- ORCID number: 0000-0001-8968-6616

Author 3

- Qingwei Ma, Ph.D
- School of Mathematics, Computer Science and Engineering, City, University of London, UK

Author 4

- Jinghua Wang, Ph.D
- School of Mathematics, Computer Science and Engineering, City, University of London, UK

Author 5

- Zhihua Xie, Ph.D
- School of Engineering, Cardiff University, Cardiff, UK

Author 6

- Sarah Marran
- School of Mathematics, Computer Science and Engineering, City, University of London, UK

Full contact details of corresponding author.

Shiqiang Yan, shiqiang.yan@city.ac.uk, 0044 20 7040 3330

School of Mathematics, Computer Science and Engineering, City, University of London

Northampton Square, London, EC1V 0HB, UK

Editor's note: your article's title and abstract are the main ways that readers will find your work. For each, aim to make them:

- *clear and interesting*
- *include keywords that your peers might type into a search engine*
- *place such keywords at the beginning of the first sentence. Google will then find them more easily*

Each keyword only needs to be mentioned once, after that use plenty of other similar words.

This is an example created from parts of other articles, it is not designed to be read for sense.

Abstract (150 – 200 words)

The paper presents a numerical investigation of the interaction between focused waves and wave energy converter (WEC) models using a hybrid solver, qaleFOAM, which couples a two-phase incompressible Navier-Stokes (NS) solver OpenFOAM/InterDyMFoam with the Quasi Lagrangian-Eulerian Finite Element Method (QALE-FEM) based on the fully nonlinear potential theory (FNPT) using the domain-decomposition approach. In the qaleFOAM, the NS solver deals with a small region near the structures (NS domain), where the viscous effect may be significant; the QALE-FEM covers the remaining computational domain (FNPT domain); an overlap (transitional) zone is applied between two domains. The WEC models, mooring system and the wave conditions are specified by the CCP-WSI (Collaborative Computational Project in Wave-Structure Interaction) Blind Test Series 2. In the numerical simulation, the incident wave is generated in the FNPT domain using a self-correction wavemaker and propagates into the NS domain through the coupling boundaries and attached transitional zones. An improved passive wave absorber is imposed at the outlet of the NS domain for wave absorption. The practical performance of the qaleFOAM is demonstrated by comparing its prediction with the experimental data, including the wave elevation, motion responses (surge, heave and pitch) and mooring load.

Keywords chosen from ICE Publishing list

Fluid Mechanics; Mathematical Modelling; Renewable Energy

List of notations (examples below)

ρ_w is the density of the water

ϕ is the velocity potential

η is the free surface elevation

$\vec{u}$ is the fluid velocity

p is the pressure

w is the weighting function ranging from 0 to 1

d is the water depth

$\vec{U}_h$ is the horizontal velocity component

U_z is the vertical velocity component

$\tilde{\omega}$ is the instantaneous wave frequency

$\tilde{k}$ is the instantaneous wave number

$\tilde{\eta}$ is the recorded wave elevation at the wave absorber

$\vec{n}_h$ is the normal direction of the absorber surface

Introduction

Reliable prediction on the structural responses in waves plays an essential role on the design, deployment and operation of the offshore and marine structures, such as the wave energy converters (WECs). For survivability of the structure, its behaviour in realistic extreme wave conditions need to be paid extra attention. Such extreme wave conditions are often generated in physical and numerical wave tanks using a focused wave group, e.g. the NewWave theory (Tromans et al. 1991). Consequently, modelling the wave-structure interaction (WSI) in focused waves attracts the interests from both the academia and industrial.

To model WSIs, numerous numerical models and software have been developed based on a wide range of theoretical models, including the fully nonlinear potential theory (FNPT), where the fluid is assumed to be incompressible, irrotational and inviscid, and the single- or multi-phase Navier-Stokes (NS) models with or without turbulence modelling. The performances of these models rely on the effectiveness of generating incident waves in the far field, modelling the wave propagation, simulating structural responses and resolving small-scale turbulence/viscous effects in the near field. For the non-breaking extreme waves, it is widely accepted that the FNPT model can satisfactorily reproduce the wave conditions and model their propagation in a large computational domain (e.g. Grilli et al., 2001; Ma et al., 2001, 2006, 2015; Ning et al., 2008, 2009; Stansby, 2013; Engsig-Karup et al., 2016; Wang et al., 2018). For simulating structural responses, the FNPT model can also deliver a promising accuracy if the structure is relatively big compared with the wave length (Celebi et al, 1998; Kashiwagi, 2000; Tanizawa and Minami,2001; Wu and Hu, 2004; Bai and Eatock Taylor, 2006; Yan and Ma, 2007; Ma and Yan, 2009; Hu et al. 2020), due to insignificant viscous effects involved in such problems. This was further confirmed by the final report of the first CCP-WSI (Collaborative Computational Project in Wave-Structure Interaction) blind test held in ISOPE 2018 (Ransley et al. 2019), in which cases with a fixed FPSO subjected to extreme wave conditions were numerically simulated using various numerical models and compared with the experimental data. The blind test minimised the possibility of numerical calibrations or tuning for the participated numerical models, due to the fact that the experimental data was released after the numerical predictions were submitted, and, therefore, largely reflects the reliabilities of participated numerical models for daily practices without available experimental data. One conclusion

given by Ransley et al (2019) is that FNPT methods have performed equally as well as the high fidelity methods; the FEM-based FNPT method, i.e. the Quasi Lagrangian Eulerian Finite Element Method (QALE-FEM, Ma & Yan, 2006,2009; Yan & Ma, 2007; Ma et al. 2015), is at least 1.5 orders of magnitude faster than the quickest NS code and has comparable predictive capability in these cases (Ransley et al. 2019), where the viscous and the turbulent effects are insignificant (Yan and Xie et al. 2019).

However, if the relative size of the structure is small compared with the characteristic wave length, e.g. within the range of the application of the Morison's equation (usually < 0.2 characteristic wavelength), the viscous effects become important. The viscous effects may also be significant when the motion of the structure is significant (e.g. Yan & Ma, 2007; Hu et al, 2020) and/or the fluid is sloshing in a confined zone (e.g. Yan and Ma et al. 2019). For such problems, the NS models may be necessary and the potential theory is not suitable, unless an appropriate artificial viscosity is applied (e.g. Yan & Ma, 2007). The artificial viscosity is often numerically calibrated using available experimental results or reliable high-fidelity predictions. This obviously brings inconvenience and uncertainty into the numerical practices. However, the NS model is more time-consuming compared with the FNPT models, as evidenced by Ransley et al. (2019), not only because of its higher degree of complexity of the governing equations, but also due to the fact that a much finer temporal-spatial resolutions are required by the former to achieve convergent results. For these reasons, the NS models are rarely applied to modelling WSIs in large spatial-temporal domain. In many applications (e.g. Hildebrandt and Sriram, 2014; Hu et al, 2014, 2017), the computational domain of the NS model is limited to a finite space near the structure (near field). This implies that one needs to accurately specify the wave field on the wave generation boundaries of the computational domain. A few tools (e.g. Jacobsen et al. 2011; Hu et al. 2014) are available for specifying the wave conditions using different wave theories, e.g. the linear wave theory, second-order wave theory, Stokes wave theory, stream functions and high-order potential theories (e.g. OceanWave3D, Engsig-Karup et al. 2008). Recently, developments on hybrid models, combining the NS solver with simplified theory, for modelling WSIs have attracted interest of world-wide researchers. They take the advantages of the simplified theories for robust modelling of large-scale wave propagations within their range of application and the advantages of the NS models on resolving small-scale viscous/turbulent effects, vortex shedding and flow separation, fluid compressibility and aeration. By limiting the computational

domain for the NS model to a small temporal/spatial zone, e.g. near the structure or where/when breaking wave occurs, they are expected to achieve robust solutions without comprising the overall computational accuracy. Broadly speaking, applying these tools with the NS models leads to a hybrid model combining these wave theories with the NS model using one-way zonal approach (space-splitting or domain decomposition). Both the function-splitting, e.g. the velocity-decomposition (Edmond et al, 2013), space-splitting /domain-decomposition (e.g. Colicchio et al, 2006; Yan and Ma, 2010a; Hildebrandt et al., 2013; Sriram et al. 2014; Fourtakas et al. 2017; Li et al. 2018; Zhang et al. 2020) and time-splitting approaches (e.g. Wang et al, 2018) have been attempted. Systematic reviews on the development of the hybrid models can be found in Sriram et al. (2014), Li et al. (2018), Wang et al. (2018) and Zhang et al (2020). The effectiveness of the hybrid model on improving the computational efficiency has been reported by recent CCP-WSI blind test for modelling the interaction between the focused wave and the floating bodies (Ransley, Yan and Brown et al, 2020). It was concluded that the hybrid methods combining the FNPT with NS solvers, including the qaleFOAM combing the QALE-FEM with openFOAM (Li et al., 2018; Yan et al 2019; Yan et al. 2020) and a one-way hybrid model combining the FNPT with SPH (Zhang et al 2020), demonstrate a potential improvement in the required CPU effort when compared to the most robust NS solvers participating to the test, including one adopting the linear and second-order wave condition in the OpenFOAM (wave2Foam, Jacobsen et al. 2011) . It is admitted that the implementations of different numerical models, e.g. the computational domain and mesh sizes, are considerably influenced by users' experiences, since no specific domain/mesh are provided for standardisation. Nevertheless, the comparison by Ransley, Yan and Brown et al. (2020) may demonstrate a better practical performance of the hybrid model for WSI problems than both the potential theory and NS solvers.

This paper contributes to the CCP-WSI Blind Test Series 2, in which the cases with two simplified WEC models subjected to focusing waves with different wave conditions are set. The details of the case configurations can be found in Ransley, Brown and Hann, et al. (2020). The sizes of the WEC models in this test are considerably smaller than the characteristic wavelength, implying that the associated viscous effect may be significant. Furthermore, one of the WEC model is a cylinder with a moonpool at its centre, in which the liquid sloshing is expected to bring additional viscous damping for supressing the wave-induced motions of the WEC model. Following Yan et al. (2020), the qaleFOAM with an improved

passive wave absorber is applied to model the cases considered in the blind test. The numerical results on the motions of the WECs have been obtained before the experimental data were released. This paper mainly focuses on the comparison with the experimental data to demonstrate the practical performance of the qaleFOAM. For this purpose, all results presented in this paper are the originally submitted ones but additional quantitative analysis is added.

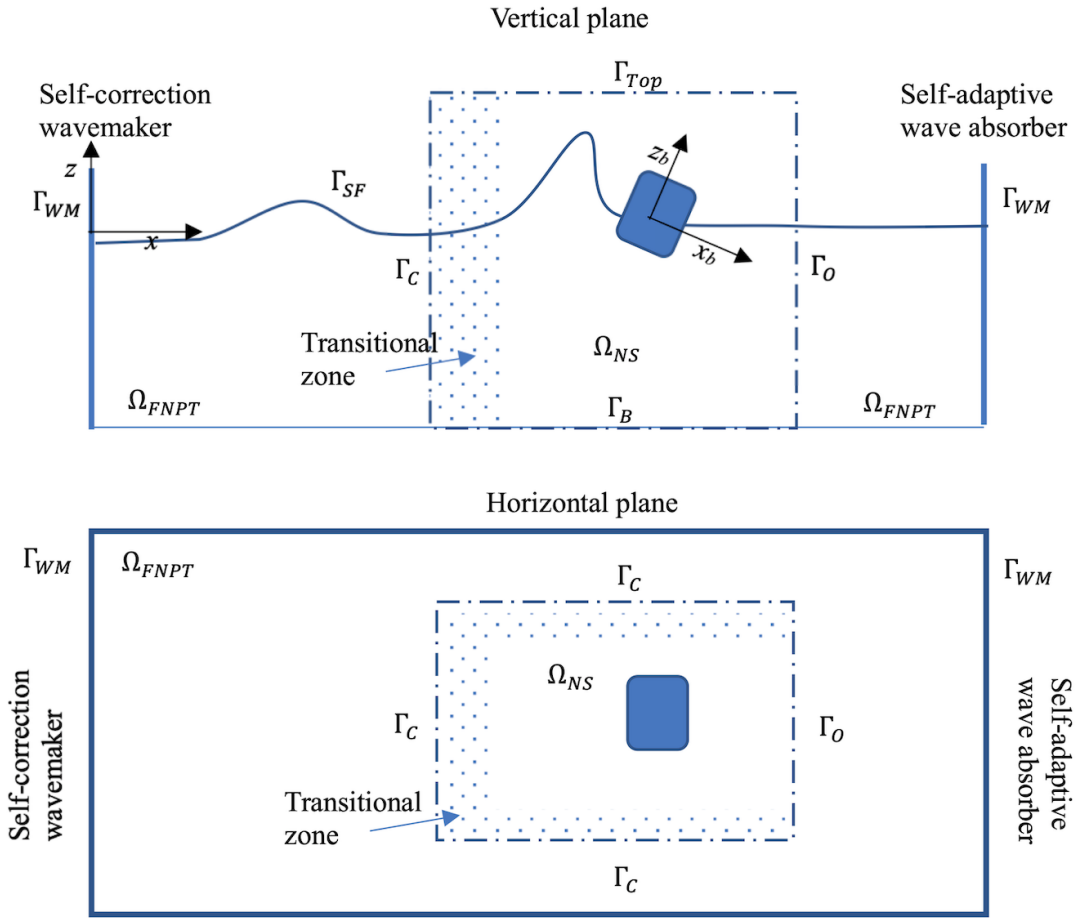

Figure 1. Schematic sketch of the domain decomposition and the coupling approach of the qaleFOAM (Ω_{FNPT} does not include the floating structure)

2. Mathematical formula

The hybrid model, qaleFOAM, combines the QALE-FEM and OpenFOAM/InterDyMFoam (Jasak, 2009) using the domain-decomposition strategy. The details of the qaleFOAM have been given by Li et al. (2018) but a summary is given herein for completeness. Figure 1 illustrates the coupling of the FNPT and NS solvers, which are combined via a coupling boundary, Γ_c. The FNPT domain (Ω_{FNPT}) starts from a location far away from the structures, where a wavemaker is used to generate the incoming wave. The

length of the FNPT domain shall be sufficient to cover the inlet of the NS domain (Ω_{NS}). In this paper, one-way coupling is adopted and, therefore, the solution in Ω_{FNPT} is only used to provide an accurate wave condition at Γ_c. This means that the diffraction and radiation caused by the structures do not need to be reproduced in Ω_{FNPT} and thus the structure is omitted from Ω_{FNPT}. The right end of Ω_{FNPT} is an absorption boundary and the self-adaptive wave absorber (Yan et al. 2016) is employed. The absorption efficiency of the absorber is approximately 95% in terms of wave energy for the case considered in this paper and is at a similar level for a wide range of nonlinear regular and irregular waves, as demonstrated by Yan et al. (2016). As all other techniques, perfect absorption is impossible and the reflection from the right end of Ω_{FNPT} exists no matter how small it is. Such reflection can influence the structural responses when it approaches the structure site. To minimise the effect, the length of Ω_{FNPT} is specified to be sufficiently long such that required duration of the results is obtained before the reflection wave reaches the structure site. In Ω_{FNPT}, the QALE-FEM is used to solve the governing equations and its high robustness on modelling nonlinear waves up to wave breaking (Yan and Ma, 2010b) assures a good overall robustness of the qaleFOAM, even though a long Ω_{FNPT} may be implemented to ensure a tolerable error caused by the reflection from the end of Ω_{FNPT} during the simulation. Ω_{NS} is bounded by the coupling boundaries Γ_c at its left end and two sides in longitude direction (dashed line in Figure 1), seabed Γ_B, a pressure inlet/outlet boundary on the top Γ_{TOP}, where the total pressure is specified as the atmospheric pressure, and the right end boundary Γ_O. In Ω_{NS}, the multiphase solver interDyMFoam, based on the finite volume method (FVM) with volume of fluid (VOF) technique for identifying the fluid phases, is used. On the coupling boundary Γ_c, the velocity and pressure for the NS solver are fed by the QALE-FEM using,

$$\vec{u}(x,y,z) = \begin{cases} \nabla\phi(x,y,z) & z \le \eta \\ (1-R_z)\nabla\phi(x,y,\eta) + R_z\vec{u}_w(x,y,z) & z > \eta \end{cases} \quad (1)$$

$$p(x,y,z) = \begin{cases} -\rho_w \dfrac{\partial\phi}{\partial t} - \rho_w \dfrac{\left|\vec{\nabla}\phi\right|^2}{2} - \rho_w g z & z \le \eta \\ 0 & z > \eta \end{cases} \quad (2)$$

in which ρ_w is the density of the water; ϕ is the velocity potential; η is the free surface elevation; $\vec{u}$ is the velocity vector and p the pressure. It is noted that the FNPT is a single-phase model only describing the

water flow. In Eq. (1), the velocity of the flow above the free surface (i.e. $z > \eta$ the air phase) is specified by a weighted summation of the corresponding water velocity on the free surface ($\nabla\phi(x, y, \eta)$) and the wind velocity, $\vec{u}_w(x, y, z)$, where R_z is a ramp function ranging from 0 to 1, to ensure a smooth transition of the fluid velocity from the water phase to the air phase. $R_z = 1 - e^{-\beta(z-z_t)/l_z}$ when the volume fraction α at a surface cell on Γc is smaller than 0.01, otherwise, $R_z = 0$, where β is an exponential coefficient, l_z is the size of the transition zone and z_t is the vertical coordinate corresponding to the upper boundary of the surface cell in which $\alpha > 0.01$. In this paper, $\vec{u}_w(x, y, z) = 0$, β = 5 and l_z equal to the vertical cell size near the free surface at Γ_c are appropriate according to the preliminary test. The volume fraction at a surface cell on Γ_c is specified by the ratio of the wetted surface area against the total area of the cell after the free surface at Γ_c is determined by η. Detailed numerical formulation may be found in Yan and Ma (2010a) and Jacobsen et al.(2011).

It is noted that Eq. (2) can be used to specify the pressure at Γ_c of Ω_{NS}, acting as a pressure boundary condition. However, applying both Eq. (1) and (2) for velocity and pressure boundary conditions at Γ_c results in a scenario that the velocity-pressure relation at such boundary follows the Bernoull's equation and thus the NS equation is not satisfied, possibly yielding a unsmoothed NS solutions near Γ_c . In the qaleFOAM, two techniques have been employed to overcome the problem. The first one is to use Eq. (1) to specify the velocity boundary condition and to impose the fixed Flux Pressure condition, available in OpenFOAM, as the pressure boundary condition. The 2nd approach is to implement a transitional zone near Γ_c. (Fig. 1), similar to the relaxation zone suggested by Jacobsen et al. (2011). In the transitional zone, the NS-solution f (velocity and pressure) is corrected by $f_{QALE}w + f_{NS}(1 - w)$, where subscripts QALE and NS stand for QALE-FEM solution and NS solution respectively; w is the weighting function, which is 1 on Γ_c, and 0 on the other boundary of the transitional zone, and the exponential function following Jacobsen et al. (2011) is employed. This does not only ensure a smooth transition of the solutions within the transitional zone, but also absorb the reflection/radiation waves from the structures. The length of the transitional zone is determined based on a preliminary test, which suggests that a length of 1 to 2 characteristic wave length is sufficient (Li et al, 2018).

The wave in the qaleFOAM is generated by the QALE-FEM in Ω_{FNPT} using a second order wavemaker theory (Schaffer, 1996) and propagates towards Ω_{NS} through the coupling boundary Γ_c,. Due to the fact

that neither the shape nor the motion of the wavemaker are specified in the blind test, to reproduce the wave conditions identical to that in the laboratory, a self-correction technique (Ma et al. 2015) is employed in this study. A summary of this technique is given here for completeness. The initial amplitudes and phases of the wave components driving the motion of the wavemaker are given by $a_i^0 = \sqrt{2S(\omega_i)\Delta\omega}$ and $\varphi_i^0 = k_i x_f - \omega_i t_f$, $i = 1, 2 \ldots N$, where x_f and t_f are the specified focusing location and time, respectively. The target spectrum $S^*(\omega)$ and phase φ^* are obtained by applying FFT to the measured surface elevation $\eta^*(t, x_r)$ at a specific gauge location x_r in the experiment. Then iterations are carried out in the following procedures: (i) At the nth iteration, the wavemaker motion is specified by using a_i^n and φ_i^n, based on the second order wavemaker theory (Schäffer, 1996), and the surface elevation $\eta^n(t, x_r)$ is recorded; (ii) The amplitude and the phase of each component are corrected by $a_i^{n+1} = a_i^n \sqrt{S^*(\omega_i)/S^*(\omega_i)}$, $\varphi_i^{n+1} = \varphi_i^n + \varphi_m^*(\omega_i) - \varphi_m^n(\omega_i)$, where the subscription m denotes the average phase within the range $[\omega_i - \Delta\omega/2, \omega_i + \Delta\omega/2]$; (iii) The error between $\eta^*(t, x_r)$ and $\eta^n(t, x_r)$ is calculated by using the formula, $Err = \max\{(\eta^* - \eta^n)^2 / \eta^{*2}\}$. If Err is sufficiently small, the iteration stops; Otherwise, $n = n + 1$, go to step (i). Although this approach seems to calibrate the wave in the observation point, numerical investigations have indicated that the wavemaker motion specified in such a way result in a satisfactory agreement between the numerical wave elevation with the experimental data at other locations (Ma et al, 2015; Yan et al, 2020).

On the right end of the NS domain, Γ_O , a fully absorption of the reflected wave from this boundary or a free passage of the incoming wave is expected. In our previous paper (Li et al. 2018), this boundary was treated in the same way as the left end. The numerical investigation by Li et al. (2018) has demonstrated the effectiveness of this approach for a satisfactory absorption of the reflected waves. However, in this paper, the improved passive wave absorber (Wang et al. 2019; Yan et al. 2020) is employed. On the boundary applying such absorber, a fixed Flux Pressure condition is imposed, the fluid velocity above the free surface (air phase) is specified by a zero-gradient condition, whereas the fluid velocity below the free surface (water phase) are given by

$$\vec{U}_h(t) = \tilde{\omega}(t) \frac{\cosh\left(\tilde{k}(t)(z+d)\right)}{\sinh\left(\tilde{k}(t)d\right)} \tilde{\eta}(t) \cdot \vec{n}_h$$

3.

193 $$\frac{\partial U_z}{\partial z} = 0$$

194 4.

195

196 where $\vec{U}_h$ and U_z are the horizontal and vertical velocity components, respectively; $\tilde{\omega}$, $\tilde{k}$, $\tilde{\eta}$ are

197 instantaneous wave frequency, wave number and the wave elevation recorded at the location of the

198 absorber; $\vec{n}_h$ is the normal direction of the absorber surface. Once $\tilde{\eta}$ is recorded, $\tilde{\omega}$ can be obtained using

199 the EKF filter and $\tilde{k}$ can be determined using the linear wave dispersion. The effectiveness of the

200 improved passive wave absorber has been demonstrated in Wang et al. (2019) and readers are referred to

201 these references for further details. For the boundary on the floating body surface, the moving-wall

202 velocity boundary condition and a zero-gradient pressure condition are imposed.

203

204 In the qaleFOAM, the NS equation, continuity equation and the transport equation for the volume fraction

205 are solved in the arbitrary Lagrangian Eulerian (ALE) forms in order to use the dynamic mesh technique.

206 After the governing equations are solved, the force and moment on the floating body can be evaluated.

207 The following six-degree-of-freedom (6DoF) motion equation is solved in a body-fixed coordinate

208 system (O_b-x_b-y_b-z_b, as sketched in Fig. 1), where the origin O_b locates at the centre of the gravity of the

209 floating body, following Yan and Ma (2007) and Ma and Yan (2009),

210

211 $$[M]\dot{\boldsymbol{U}}_c = \boldsymbol{F}$$

212 5.

213 $$[I]\dot{\boldsymbol{\Omega}} + \boldsymbol{\Omega} \times [I]\boldsymbol{\Omega} = \boldsymbol{N}$$

214 6.

215 $$\frac{d\boldsymbol{S}}{dt} = \boldsymbol{U}_c$$

216 7.

217 $$[B]\frac{d\boldsymbol{\theta}}{dt} = \boldsymbol{\Omega}$$

218 8.

219 where F and N are the external forces and moments acting on the floating body in the body-fixed coordinate

220 system; $\boldsymbol{U}_c$ and $\dot{\boldsymbol{U}}_c$ are translational velocity and acceleration at its gravitational centre (rotational centre);

$\boldsymbol{\Omega}$ and $\dot{\boldsymbol{\Omega}}$ are its angular velocity and acceleration; $\boldsymbol{\theta}(\alpha, \beta, \gamma)$ are the Euler angles and $\boldsymbol{S}$ is the translational displacement. In Eq. (5) and (6), $[M]$ and $[I]$ are the mass and inertia-moment matrices, respectively. $[B]$ in Eq. (8) is the transformation matrix formed by Euler angles and defined as

$$[B] = \begin{bmatrix} cos\beta cos\gamma & sin\gamma & 0 \\ -cos\beta sin\gamma & cos\gamma & 0 \\ sin\beta & 0 & 1 \end{bmatrix}$$

It is easy to deduce that $\boldsymbol{\Omega} \times [I]\boldsymbol{\Omega} = \mathbf{0}$ and $[B]$ is a unit matrix for the cases with 3 DoF, i.e. surge, heave and pitch. After the translational and rotational motions of the floating body are obtained by Eqs. (5-8), the OpenFOAM mesh will be updated using the dynamic mesh technique.

Table 1 Wave Condition

Case ID	An(m)	fp(Hz)	h(m)	Hs(m)	kA
1BT2	0.25	0.3578	3.0	0.274	0.128778
2BT2	0.25	0.4	3.0	0.274	0.160972
3BT2	0.25	0.4382	3.0	0.274	0.193167

Table 2 Mass and Moment of Inertia

Model	m(kg)	Z_{C0M}(m)	I_{xx}(kgm²)	I_{yy}(kgm²)	I_{zz}(kgm²)
1	43.674	0.191	1.620	1.620	1.143
2	61.459	0.152	3.560	3.560	3.298

3. CCP-WSI Blind Test

For all cases considered by the CCP-WSI blind test, the experiment was performed in the wave basin at the University of Plymouth, which features 35 m in length, 15.5m in width and 3m in depth. Flap wave paddles are installed to generate three-dimensional waves. The temporal variation of surface elevations at various locations is recorded by 13 wave gauges (WG) with sampling frequency of 128Hz. The sketches of the geometry of the wave basin and the distribution of the gauges can be found in Ransley, Brown and Hann et al (2020) . Three wave conditions are used and summarized in Table 1. Two models of point-absorber WECs with a specific mooring system are initially placed at where WG5 is located. The geometries of these models are illustrated by Ransley, Brown and Hann et al (2020). The mass (m), moments of inertias (I_{xx}, I_{yy} and I_{zz}) at the centre of the mass (CoM) are summarised in Table 2, in which Z_{C0M} stands for the vertical distance from the CoM to the bottom of the models. For both models, the mooring line is a linear spring with a stiffness of 67 N/m and a rest length of 2.224 m.

3.1 Wave generation and absorption

For all wave conditions, the corresponding empty-tank simulation are carried out to examine whether the target waves are generated properly. The wave is generated using the self-correction wavemaker in the left end of Ω_{FNPT} aiming to reproduce the same time history of the wave elevations recorded at WG5. In the empty tank test, Ω_{FNPT} starts from the wavemaker and the length of Ω_{FNPT} is 50 m, which is longer than the physical wave tank. As indicated above, this is to minimise the error caused by the reflection from the right end of Ω_{FNPT}, where a self-adaptive wave absorber is imposed and produces approximately 95% absorption efficiency. Ω_{NS} starts at x = 11.55 m, between WG1 and WG2. Generally speaking, the length of Ω_{NS} shall be sufficient to accommodate the transitional zone, whose thickness is 1.5 m in the front side and 0.5 m near the size boundaries of $\Omega_{NS,}$ according to the preliminary investigations. To investigate the absorption efficiency of the improved passive wave absorber applied at the right end of Ω_{NS}, Ω_{NS} ends at x = 17.55 m, where WG8 is placed. Using such a configuration, the gauge data at WG8 can be used as a reference to qualify the absorption efficiency. The height and width of Ω_{NS} are 6m and 3m respectively. For all cases, a laminar model is specified as the turbulence properties.

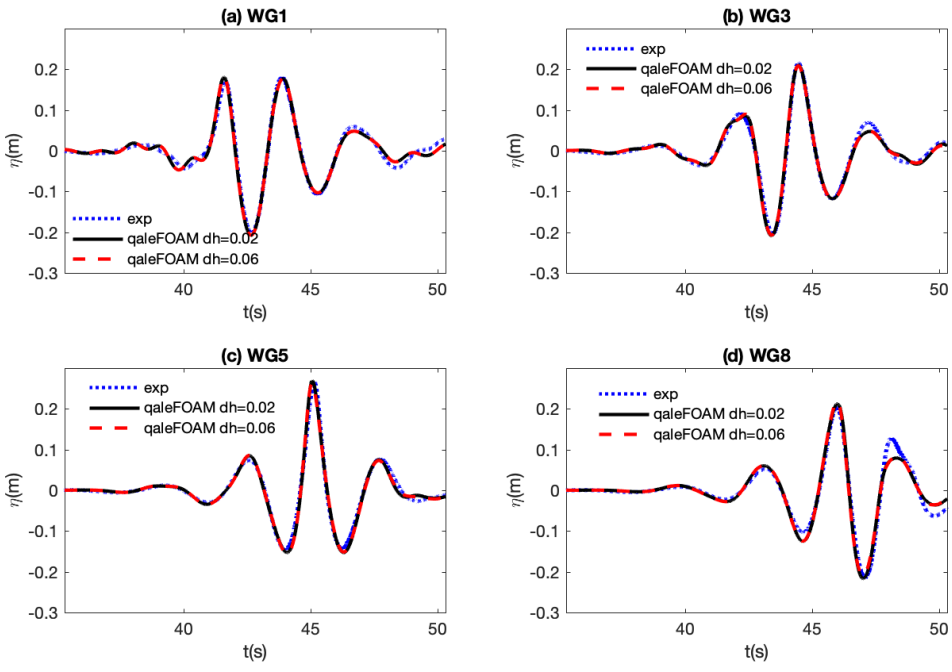

Figure 2. Comparison of the wave elevation recorded at different locations (case 1BT2, empty tank test, d_{sv} = 0.0175m)

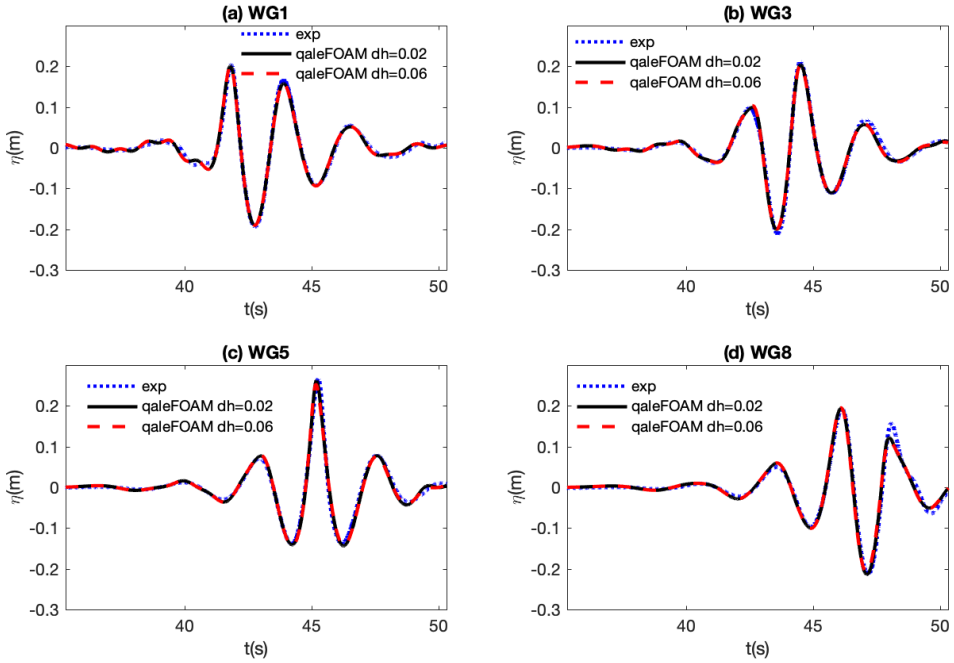

Figure 3. Comparison of the wave elevation recorded at different locations (case 2BT2, empty tank test, d_{sv} = 0.0175m)

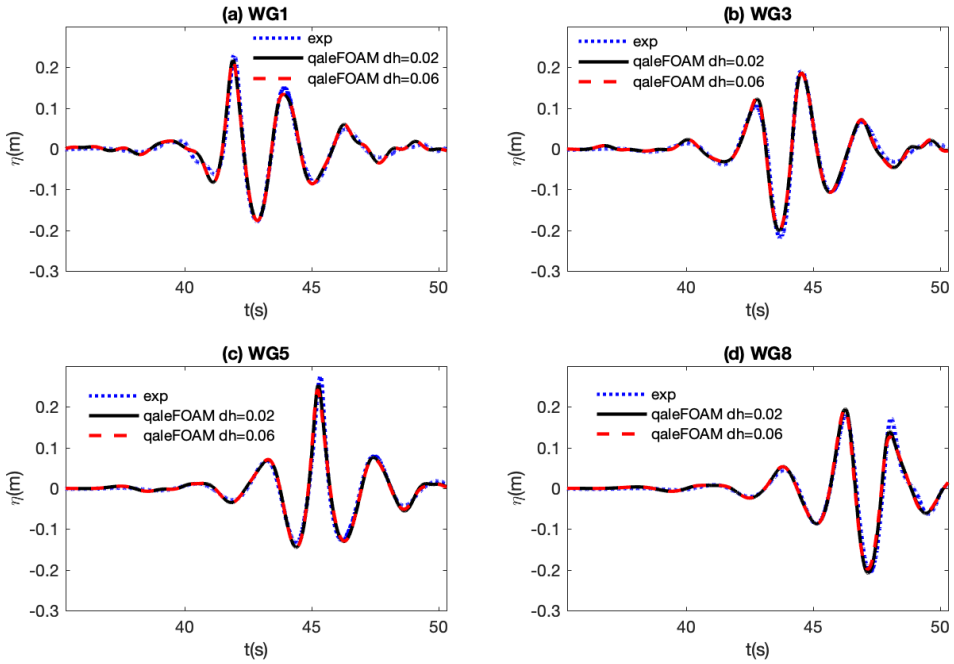

Figure 4 Comparison of the wave elevation recorded at different locations (case 3BT2, empty tank test, d_{sv} = 0.0175m)

The comparisons of the wave elevations at different wave gauges between the qaleFOAM results and the experimental data are shown in Figures 2-4, where the qaleFOAM results with two different mesh resolutions are plotted. As observed, two sets of the qaleFOAM results are almost identical to each other, demonstrating a satisfactory convergence of the qaleFOAM in the empty-tank test. More importantly, the qaleFOAM results agree well with the corresponding experimental data. This conforms a satisfactory reproduction of the target waves at WG5 by the self-correction wavemaker technique, even though the tank geometry and the wavemaker used in the qaleFOAM are different from the experiment.

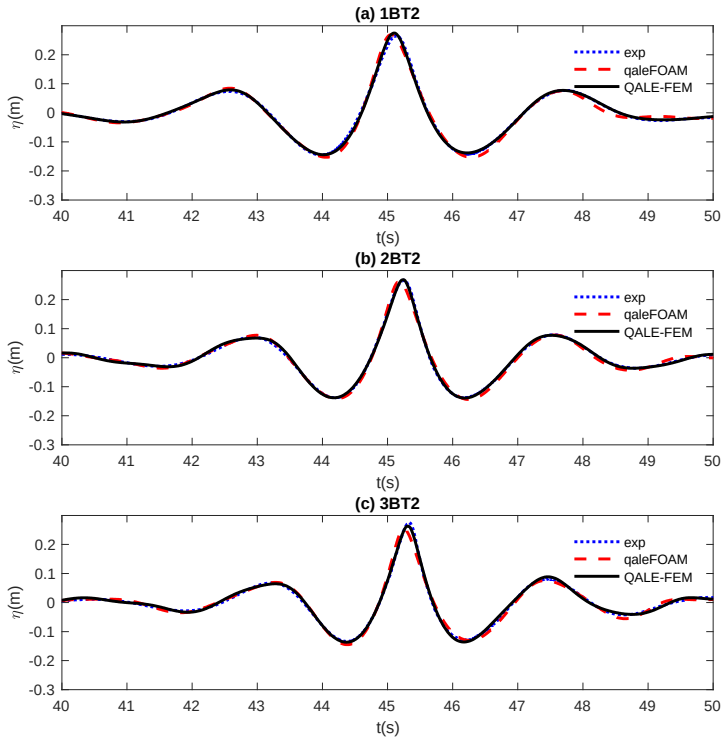

Figure 5 Comparison of the wave elevation recorded at WG5 (empty tank test, qaleFOAM: d_{sh} = 0.05m, d_{sv} = 0.0175m; QALE-FEM: ds = 0.075m)

Although the agreements between the qaleFOAM results and the experimental data at WG5 has proven that the present passive wave absorber applied at Γ_O can effectively prevent the wave reflected at Γ_O from influencing the wave condition at WG5 during the required duration of the simulation (the blind test requires the submission of the time history ranges from 35.3 s to 50.3 s), a further analysis has been carried out to quantitively evaluate the absorption efficiency. As stated by Yan et al (2016), the theoretical approach based on the linear regular wave theory may not be applicable to highly nonlinear focusing waves considered in this paper, the absorption efficiency is estimated through the relative difference between the numerical results adopting the absorber and a reference data which does not

include reflection wave, e.g. the corresponding results obtained using a longer tank. One may agree that the wave elevation in Ω_{FNPT} by the QALE-FEM can be regarded as the refence data, since Ω_{FNPT} is sufficiently long and the reflection wave from the end of Ω_{FNPT} does not reach WG8 at t = 50.3 s. Figures 5 and 6 compare the wave elevations record at WG5 and WG8, respectively. As observed from Figure 5, the qaleFOAM results are very close to the corresponding QALE-FEM results. The relative differences between them during t = 35.3 s to 50.3 s are all within 2% for three cases (yielding an absorption efficiency of 98%). Nevertheless, at WG8 (Figures 6), the QALE-FEM results agree with the experimental data, whereas the qaleFOAM with the wave absorber results in a slightly different results from others due to the reflection from Γ_O . The relative difference between the QALE-FEM results and the qaleFOAM results are 2%, 4% and 6% (yielding absorption efficiencies of 98%, 96% and 94%) for cases 1BT2, 2BT2 and 3BT2, respectively. This is consistent with what Yan et al (2020) concluded.

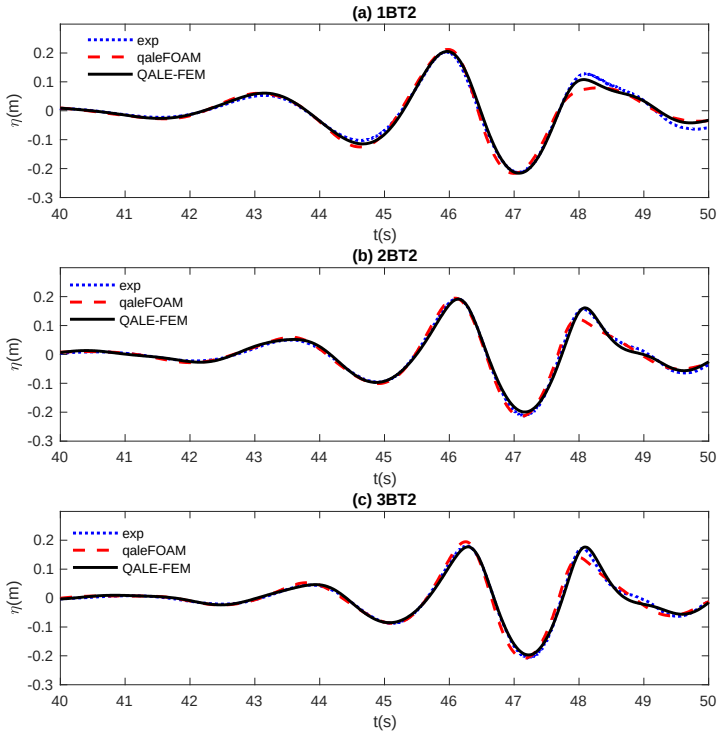

Figure 6 Comparison of the wave elevation recorded at WG8 (empty tank test, qaleFOAM: d_{sh} = 0.05m, d_{sv} = 0.0175m; QALE-FEM: ds = 0.075m)

3.2 Mesh Convergent Test

The results shown in Figures 2-6 are obtained in a wave tank without WEC models. For the cases with WECs, mesh convergent tests are also carried out. For each WEC model, four sets of computational mesh are generated using the snappyHexMesh tool and adopted in the convergent test. The horizontal (d_{sh}) and vertical grid sizes (d_{sv}), the total number of grid, N_t, and the number of grid on the structure surface, N_s, are

summarised in Table 3. In order to capture the nonlinear wave-structure interaction, as well as small-scale viscous effects, e.g. boundary layer seperation, near the structure, the mesh near a confined zone surrounding the WEC model with a radius of 0.5m is refined. One example of the mesh near the WEC is illustrated in Figure 7.

Table 3 Summary of computational grids used in the convergent test

Model	Mesh	d_{Sh}(m)	d_{Sv} (m)	N_t (M)	N_s
1	Finest	0.04	0.015	1.550	10348
1	Fine	0.05	0.0175	0.956	7512
1	Medium	0.06	0.02	0.613	5346
1	Coarse	0.08	0.02	0.358	3882
2	Finest	0.04	0.015	1.549	20128
2	Fine	0.05	0.0175	0.937	13920
2	Medium	0.06	0.02	0.612	9840
2	Coarse	0.08	0.02	0.376	7244

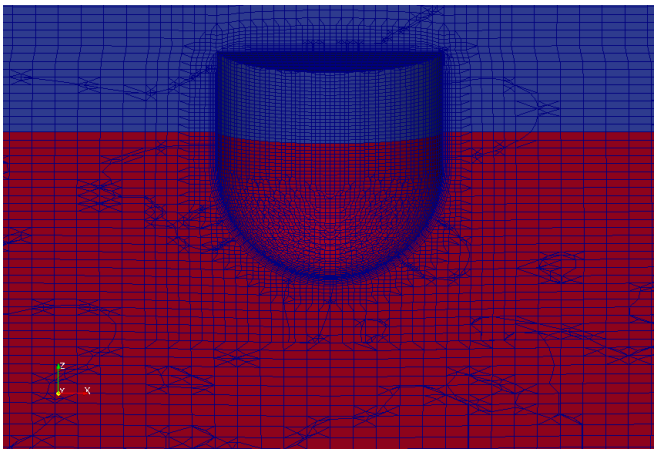

Figure 7 Illustration of the computational mesh near the WEC (Model 1, d_{sh} = 0.05m, d_{sv} = 0.0175m, red: water; blue: air)

Figure 8 and Figure 9 compare the motions of and the mooring force on the WEC model 1 and model 2, respectively, subjected to the wave condition 3BT2, which has the highest wave steepness (kA = 0.193127) within all wave conditions specified by the blind test. It is observed that the present results are insensitive to the mesh resolutions for all participated mesh; especially the results with medium mesh satisfactorily agree with the corresponding results with finer mesh. Relative errors of the qaleFOAM results with different mesh sizes are quantitatively analysed. Some results are summarised in Table 4, in which the relative errors of the numerical results with medium mesh in terms of both the peak value (E_p) and the RMS error using the time histories during t = 35.3 s to t = 50.3 s. Similar to Brown et al. (2020), the results with finest mesh are regarded as the reference values for the analysis. Considering the fact that

the maximum relative errors shown in Table 4 is RMS error of 7.5% for Model 1 subjected to Wave 2BT2, one may agree that the medium mesh is sufficient to achieve convergent predictions on the WEC motions and the mooring force, although similar numerical uncertainty analysis by Brown et al. (2020) is not presented.

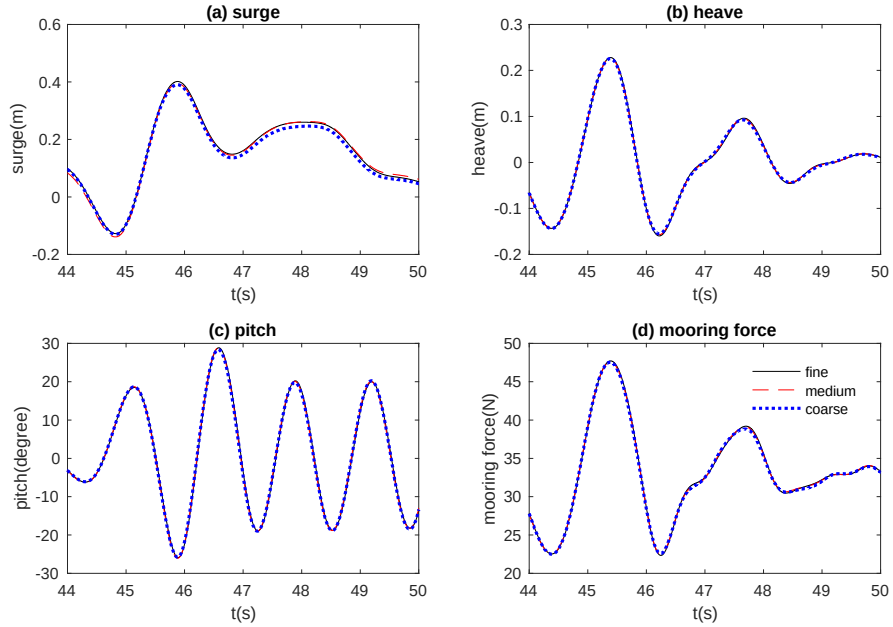

Figure 8 Comparison of the WEC motions and mooring force in the cases with different mesh sizes (case 3BT2, Model 1)

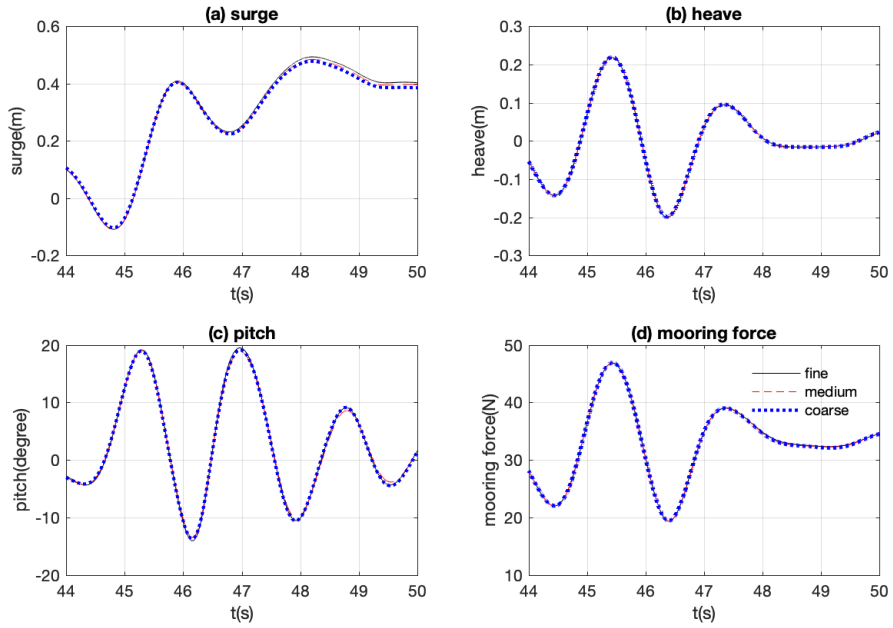

Figure 9 Comparison of the WEC motions and mooring force in the cases with different mesh sizes (case 3BT2, Model 2)

345 Table 4 Relative error of qaleFOAM results with the medium mesh

Error (%)	Model 1 1BT2	Model 1 2BT2	Model 1 3BT2	Model 2 1BT2	Model 2 2BT2	Model 3 3BT2
E_P (Surge)	0.17	2.53	1.69	0.49	0.84	1.83
E_P (Heave)	0.81	1.05	0.69	0.30	0.22	0.18
E_P (Pitch)	0.27	0.39	0.71	0.44	1.12	2.48
E_P (Force)	0.32	0.44	0.27	0.15	0.08	0.10
RMS(Surge)	5.22	7.47	5.36	1.60	1.12	1.75
RMS(Heave)	1.06	1.90	1.91	0.79	0.97	0.49
RMS(Pitch)	2.08	4.97	4.11	3.53	3.38	3.60
RMS(Force)	0.18	0.28	0.26	0.14	0.15	0.16

346

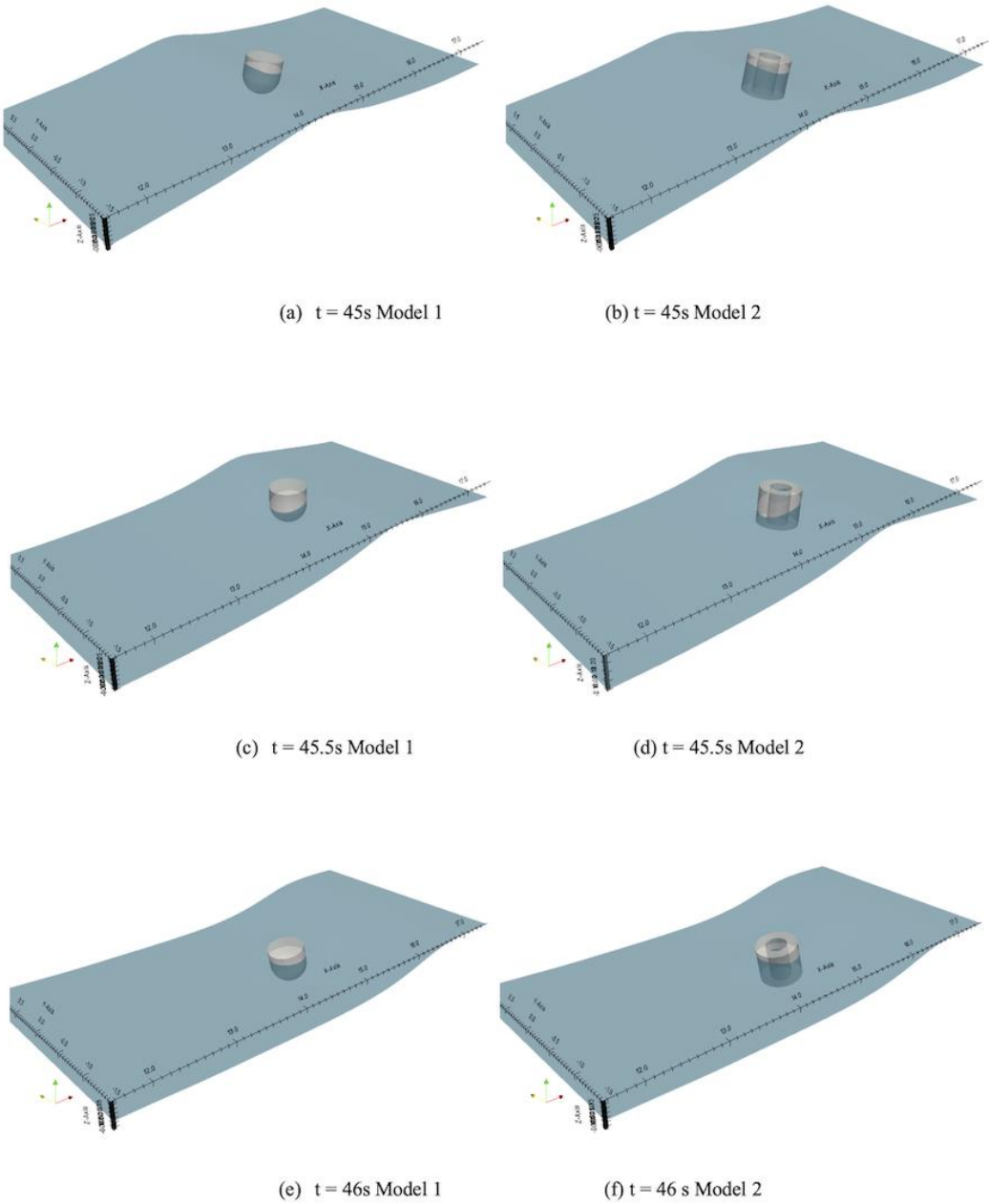

(a) t = 45s Model 1 (b) t = 45s Model 2

(c) t = 45.5s Model 1 (d) t = 45.5s Model 2

(e) t = 46s Model 1 (f) t = 46 s Model 2

347

348 Figure 10 Wave elevations near the WECs at t = 45s (case 2BT2)

3.3 Responses of WECs in extreme waves

By using the medium mesh, the motions of the WECs subjected to three wave conditions are numerically simulated and analysed in this section. For demonstration, Figure10 illustrates the free surface profiles near the WEC modelsat three instants around the focusing time, i.e. t = 45s, t = 45.5s and t = 46s, in the cases with wave condition 2BT2. As expected, the presences of the WECs do not seem to disturb the surrounding wave field, confirming to the typical feature of slender bodies (the sizes of the WECs considerably smaller than the characteristic wavelength).

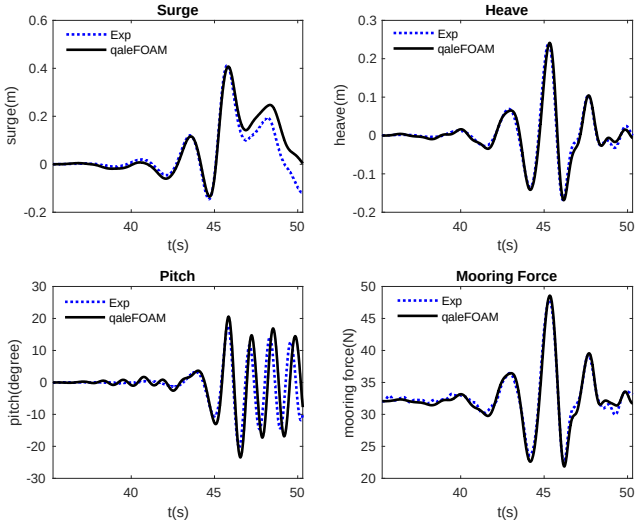

(a) Model 1

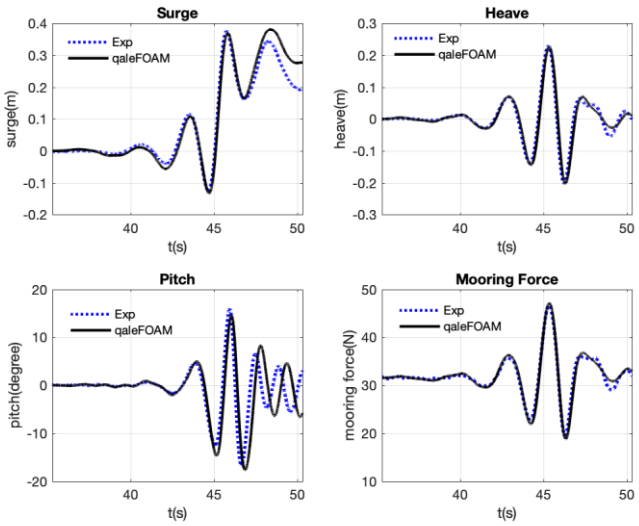

(b) Model 2

Figure 11 Comparison of the time histories of the WEC motions and the mooring loads (case 2BT2)

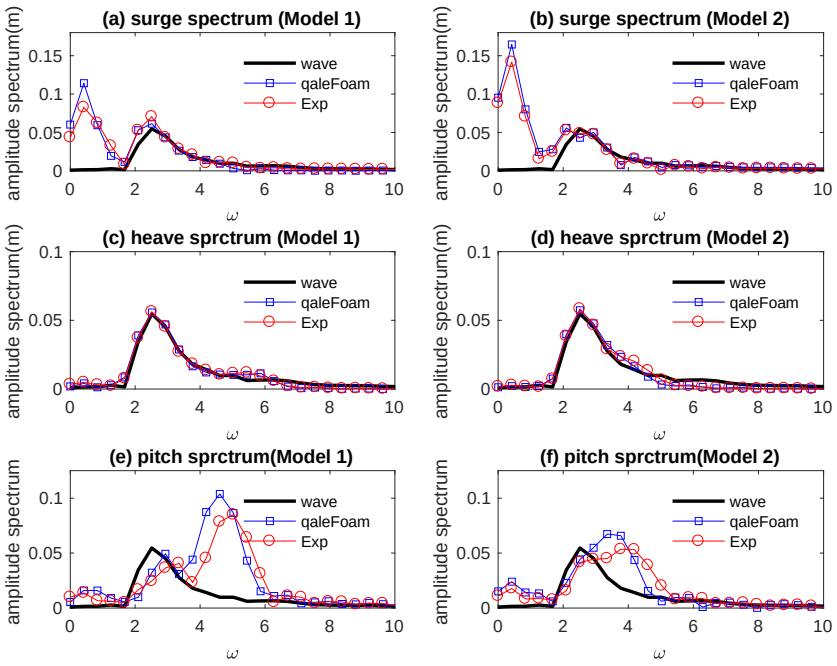

Figure 12 Comparison of the amplitude spectra of the WEC motions (case 2BT2)

Table 5 Relative error of qaleFOAM results with reference to the experimental data

Error (%)	Model 1 1BT2	Model 1 2BT2	Model 1 3BT2	Model 2 1BT2	Model 2 2BT2	Model 3 3BT2
E_P (Surge)	6.94	1.36	7.52	6.20	1.14	7.39
E_P (Heave)	9.77	0.54	3.53	3.41	1.38	1.31
E_P (Pitch)	44.0	16.4	19.9	6.38	8.51	6.75
E_P (Force)	4.72	1.59	0.86	3.45	0.87	2.00

The motions of the WECs and the mooring force acting on the WECs in the case shown in Figures 10 are illustrated in Figure 11. It is found that the profiles of the heave motions largely follow the wave motion (Figure 5(b)). This can be confirmed by Figure 12, which displays the amplitude spectra of the WEC motions and the corresponding wave spectrum at WG5 where the WECs are initially located. The spectra shown in Figure 12 are obtained using the time histories at the duration of 35.3 – 50.3s with a sampling frequency of 128Hz. As observed from Figure 12(c and d), the amplitude spectra of the wave and the heave motion are very close, suggesting a linear heave response to the incident wave. However, the surge motion and the pitch motion exhibit different features from the expected wave at the WEC sites. Specifically, the surge motions suffer from a long-period oscillation after the focused wave crest passes the WECs at $t \approx 45s$ (Figure 11 (a)), whereas the pitch motion exhibits a high-frequency response, which

379 is gradually supressed in the case with Model 2. These are confirmed by the corresponding spectrum
380 analysis shown in Figure 12 (a and b) and (e and f), respectively.
381

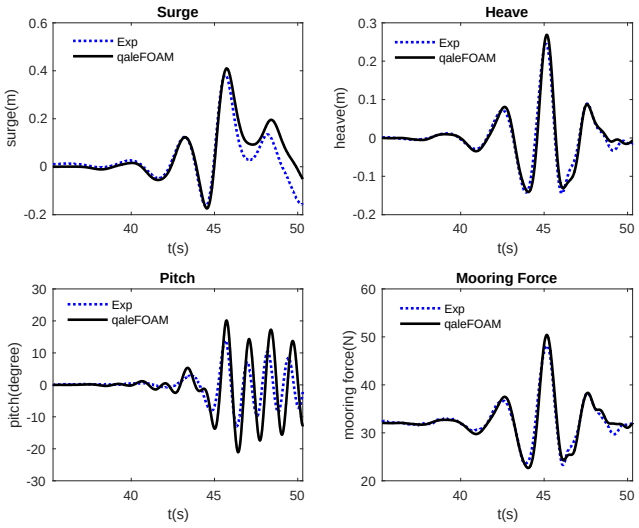

382
383 (a) Model 1

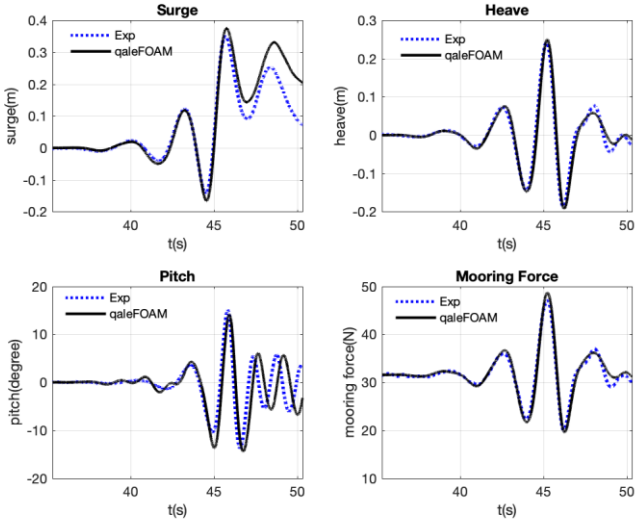

384
385 (b) Model 2
386 Figure 13 Comparison of the time histories of the WEC motions and the mooring loads (case 1BT2)
387
388

389 More importantly, the comparisons between the qaleFOAM results and the corresponding experimental
390 data shown in Figure 11 and Figure 12 largely reflect the practical performance of the qaleFOAM on
391 modelling the motions of the WECs in extreme waves. For three motion modes and the mooring loads,
392 the qaleFOAM seems to satisfactorily capture the peak values. The corresponding errors are summarised
393 in Table 5. Except the pitch motion, the relative errors on surge, heave and mooring load are all below
394 2%. However, the relative error on peak pitch angle is 16.4% and 8.51% for Model 1 and 2 subjected to

Wave 2BT2. Not only the peak pitch angle, the spectra shown in Figure 12 (e) and (f) and the corresponding time histories shown in Fig. 11 have revealed an unsatisfactory prediction by the qaleFOAM. Similar phenomena are observed in other cases with different wave conditions. The corresponding motion responses and the mooring loads are shown in Figures 13-14 and the quantitative errors on the peak values are summarised in Table 5. In fact, numerical results by other numerical methods in Ransley et al (2020) behave similarly in terms of predicting pitch motion. A recent sensitivity analysis by Windt et al (2020) has shown that the pitch motion is sensitive to the centre of rotation and the moment of inertia. Ransley et al (2020) did not provide the free-decay test for pitch motion and, therefore, it is difficult to quantify whether the error in pitch motion is due to incorrect measure of the centre of rotation and the moment of inertia.

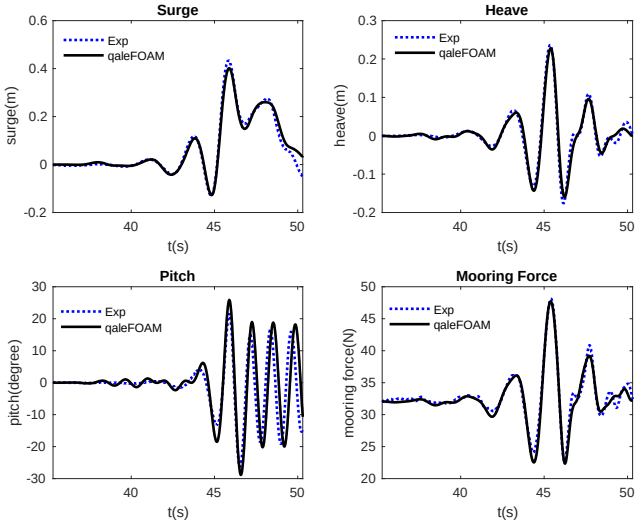

(a) Model 1

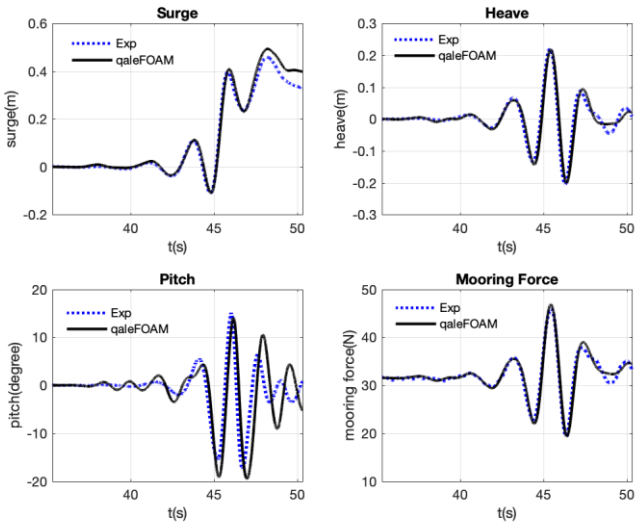

(b) Model 2

Figure 14 Comparison of the time histories of the WEC motions and the mooring loads (case 3BT2)

4. Conclusions

In this paper, the qaleFOAM is used to numerically simulate the cases specified by the CCP-WSI Blind Test 2 (Ransley, Brown et al, 2020). All wave conditions summarised in Table 1 have been considered. The effectiveness of the qaleFOAM on modelling focused wave group is assessed by comparing the wave elevations in the empty tank tests, in which the WEC models are not placed. The results confirm a promising accuracy of the qaleFOAM on modelling highly nonlinear water waves. In addition, the convergence test has demonstrated a good convergence property in terms of predicting the motions of the WECs and the associated mooring forces. The comparisons on the motion responses of the WECs between the present numerical results and the experimental data demonstrate a satisfactory accuracy of the qaleFOAM for modelling the highly nonlinear WSI problems addressed in this paper.

It is further noted that the CPU time spent on cases 1BT3, 2BT3 and 3BT3 to achieve convergent results during t = 35.3s and t = 50.3s are, respectively 12 hours using an 8-processor MPI parallel computing in a workstation with Intel Xeon E5-2680, 2.4GHz, 32G RAM. This demonstrates a satisfactory robustness of the present qaleFOAM.

Acknowledgements

The authors gratefully acknowledge the financial support of EPSRC projects (EP/M022382, EP/N006569 and EP/N008863) and UKIERI-DST project (DST-UKIERI-2016-17-0029).

References

Bai W, Eatock Taylor R (2006) Higher-order boundary element simulation of fully nonlinear wave radiation by oscillating vertical cylinders. Applied Ocean Research, 28:247–265.

Brown SA, Ransley EJ, Greaves DM (2020) Assessing focused wave impacts on floating WECs using OpenFOAM, Proceedings of the Institution of Civil Engineers - Engineering and Computational Mechanics (in review).

Celebi MS, Kim MH, Beck RF (1998) Fully nonlinear 3D numerical wave tank simulation. Journal of Ship Research, 42:33–45.

438 Colicchio G, Greco M, Faltinsen OM (2006) A BEM-level set domain-decomposition strategy for non-
439 linear and fragmented interfacial flows. International Journal for Numerical Methods in engineering,
440 67: 1385-1419.
441 Edmund DO, Maki KJ and Beck RF (2013) A velocity-decomposition formulation for the incompressible
442 Navier–Stokes equations. Computational Mechanics, 52: 669–680.
443 Engsig-Karup AP, Bingham HB and Lindberg O (2008) An efficient flexible-order model for 3D
444 nonlinear water wave, Journal of computational physics, 228: 2100-2118.
445 Engsig-Karup AP, Eskilsson C and Bigoni D (2016) A Stabilised Nodal Spectral Element Method for
446 Fully Nonlinear Water Waves, Journal of Computational Physics, 318: 1-21.
447 Fourtakas G, Stansby PK, Rogers BD et al. (2017) On the coupling of Incompressible SPH with a Finite
448 Element potential flow solver for nonlinear free surface flows, Proceedings of the 27th International
449 Offshore and Polar Engineering Conference, San Francisco, USA.
450 Grilli ST, Guyenne P and Dias F (2001) A fully non-linear model for three-dimensional overturning
451 waves over an arbitrary bottom, International Journal for Numerical Methods in Fluids, 35(7): 829-
452 867.
453 Hildebrandt A and Sriram V (2014) Pressure distribution and vortex shedding around a cylinder due to a
454 steep wave at the onset of breaking from physical and numerical modeling, Proceedings of the 24th
455 International Offshore and Polar Engineering Conference, Vol.3, 405-410, Busan, Korea.
456 Hu ZZ, Greaves D and Raby A (2014) Simulation of extreme free surface waves using OpenFoam, 5th
457 Conference on the application of physical modelling to port and coastal protection, Varna, Bulgaria.
458 Vol. 2: 243-252.
459 Hu ZZ, Mai T, Greaves D et al. (2017) Investigations of Offshore breaking Wave Impacts on a large
460 offshore Structure, Journal of Fluids and Structure, 75: 99-116.
461 Hu ZZ, Yan S, Greaves D et al. (2020) Investigation of Interaction between extreme waves and a moored
462 FPSO using FNPT and CFD solvers, Ocean Engineering, in review.
463 Jacobsen NG, Fuhrman DR and Fredsøe J (2011) A wave generation toolbox for the opensource CFD
464 library: OpenFoam. International Journal for Numerical Methods in Fluid 70:1073-1088.
465 Jasak H (2009) OpenFOAM: Open source CFD in research and industry. International Journal of Naval
466 Architecture & Ocean Engineering, 1(2):89-94.

Kashiwagi M (2000) Nonlinear simulations of wave-induced motions of a floating body by means of the mixed Eulerian–Lagrangian method. Proceedings of the Institution of Mechanical Engineers. Part C, Journal of Mechanical Engineering Science, 214:841–855.

Li Q, Wang JH, Yan S et al. (2018) A Zonal Hybrid Approach Coupling FNPT with OpenFOAM for Modelling Wave-Structure Interactions with Action of Current. Ocean System Engineering 8: 381-407, 2018.

Ma QW, Wu GX and Eatock Taylor R (2001) Finite element simulation of fully nonlinear interaction between vertical cylinders and steep waves. Part 1: Methodology and numerical procedure. Journal for Numerical Methods in Fluid 36:265-285.

Ma QW and Yan S (2006) Quasi ALE finite element method for nonlinear water waves. Journal of Computational Physics 212: 52-72.

Ma QW and Yan S (2009) QALE-FEM for numerical modelling of non-linear interaction between 3D moored floating bodies and steep waves. International Journal for Numerical Methods in Engineering 78:713-756.

Ma QW, Yan S, Greaves D, Mai T et al. (2015) Numerical and experimental studies of Interaction between FPSO and focusing waves. The Twenty-fifth International Ocean and Polar Engineering Conference, Kona, Hawaii, USA.

Ning DZ, Teng B, Eatock Taylor R, et al. (2008) Numerical simulation of nonlinear regular and focused waves in an infinite water-depth, Ocean Engineering, 35(8-9): 887-899.

Ning DZ, Zang J, Liu SX et al. (2009) Free surface and wave kinematics for nonlinear focused wave groups, Ocean Engineering, 36(15-16): 1226-1243.

Ransley EJ, Brown SA and Hann M et al. (2020) Focused wave interactions with floating structures: A blind comparative study, Proceedings of the Institution of Civil Engineers - Engineering and Computational Mechanics (in review).

Ransley EJ, Yan S, Brown SA et al. (2019) A blind comparative study of focused wave interactions with a fixed FPSO-like structure (CCP-WSI Blind Test Series 1). International Journal of Offshore and Polar Engineering 29:113-128.

Ransley EJ, Yan S, Brown SA et al. (2020) A blind comparative study of focused wave interactions with floating structures (CCP-WSI Blind Test Series 3), International Journal of Offshore and Polar Engineering, 30(1): 1-10.

497 Schaffer HA (1996) Second-order wavemaker theory for irregular waves. Ocean Engineering 23: 47-88.
498 Stansby PK (2013) Coastal Hydrodynamics – present and future, Journal of Hydraulic Research, 51(4):
499 341-350.
500 Sriram V, Ma QW and Schlurmann T (2014) A hybrid method for modelling two dimensional non-
501 breaking and breaking waves, Journal of Computational Physics, 272: 429-454.
502 Tanizawa K, Minami M (2001) Development of a 3D-NWT for simulation of running ship motions in
503 waves. International Workshop on Water Waves and Floating Bodies, Hiroshima, Japan.
504 Tromans PS, Anaturk AR and Hagemeijer P (1991) A new model for the kinematics of large ocean
505 waves – application as a design wave. The First International Offshore and Polar Engineering
506 Conference. Edinburgh, UK, 1991.
507 Wang, JH, Ma, QW, Yan, S (2018) A hybrid model for simulating rogue waves in random seas on a large
508 temporal and spatial scale, Journal of Computational Physics, 313: 279-309.
509 Wang JX, Wang JH, Yan S et al. (2019) An improved passive wave absorber for FNPT-NS solver.
510 Twenty-ninth International Ocean and Polar Engineering Conference, Honolulu, Hawaii, USA,
511 Windt C, Schmitt P, Davidson J et al (2020) Wave-structure interaction of wave energy converters: a
512 sensitivity analysis, Proceedings of the Institution of Civil Engineers - Engineering and Computational
513 Mechanics (in review).
514 Wu GX, Hu ZZ (2004). Simulation of nonlinear interactions between waves and floating bodies through a
515 finite-element based numerical tank. Proceedings of the Royal Society of London, Series A,
516 460:3037–3058.
517 Yan S and Ma QW (2007) Numerical simulation of fully non-linear interaction between steep waves and
518 2D floating bodies using the QALE-FEM method. Journal of Computational Physics 221:666–692.
519 Yan S, Ma QW (2010a) Numerical simulation of interaction between wind and 2D freak waves. European
520 Journal of Mechanics, B/Fluids, 29(1): 18-31.
521 Yan S, Ma QW (2010b) QALE-FEM for modelling 3D overturning waves, International Journal for
522 Numerical Methods in Fluids, 63: 743-768.
523 Yan S, Ma QW, Wang JH et al. (2016) Self-adaptive wave absorbing technique for nonlinear shallow
524 water waves. ASME 35th International Conference on Ocean, Offshore and Arctic Engineering,
525 Busan, South Korea.

526 Yan S, Ma QW, Wang JH et al. (2019) Numerical modelling of wave resonance in a narrow gap between
527 two floating bodies in close proximity using a hybrid model. 38th International Conference on Ocean,
528 Offshore and Arctic Engineering, Glasgow, Scotland, OMAE2019-95247.
529 Yan S, Wang JH, Wang JX et al. (2020) CCP-WSI blind test using qaleFOAM with an improved passive
530 wave absorber, International Journal of Offshore and Polar Engineering, 30(1): 43-52.
531 Yan S, Xie ZH, Li Q et al. (2019) Comparative numerical study on focusing wave interaction with FPSO-
532 like structure. International Journal of Offshore and Polar Engineering 29: 149-157.
533 Zhang NB, Yan S, Zheng X et al. (2020) A 3D hybrid model coupling SPH and QALE-FEM for
534 simulating nonlinear wave-structure interaction, International Journal of Offshore and Polar
535 Engineering, 30(1): 11-19.
536
537
538